Stability of Active Mantle Upwelling Revealed by Net Characteristics of Plate Tectonics

Clinton P. Conrad[1*], Bernhard Steinberger[2,3], Trond H. Torsvik[3,4,5]

[1] Department of Geology and Geophysics, SOEST, University of Hawaii at Manoa, Honolulu, HI 96822, USA

[2] Helmholtz Centre Potsdam, GFZ German Research Centre for Geosciences, 14473 Potsdam, Germany

[3] Centre for Earth Evolution and Dynamics (CEED), University of Oslo, 0316 Oslo, Norway

[4] Geodynamics, Geological Survey of Norway, NO-7491, Trondheim, Norway

[5]School of Geosciences, University of Witwatersrand, WITS 2050, South Africa

* Corresponding Author (clintc@hawaii.edu)

Viscous convection within Earth's mantle is linked to tectonic plate motions[1-3] and deforms Earth's surface across wide areas[4-6]. Such close links between Earth's surface geology and its deep mantle dynamics presumably operated throughout Earth history, but are difficult to investigate for past times because the history of mantle flow is poorly known[7]. Here we show that the time-dependence of global-scale mantle flow can be deduced from the net behavior of surface plate motions. In particular, we tracked the geographic locations of net convergence and divergence for harmonic degrees 1 and 2 by computing the dipole and

quadrupole moments of plate motions from tectonic reconstructions[8,9] extended back to the early Mesozoic. For present-day plate motions, we find dipole convergence in eastern Asia and quadrupole divergence in both central Africa and the central Pacific. These orientations are nearly identical to the dipole and quadrupole orientations of underlying mantle flow, which indicates that these "net characteristics" of plate motions reveal deeper flow patterns. The positions of quadrupole divergence have not moved significantly during the past 250 Myr, which suggests long-term stability of mantle upwelling beneath Africa and the Pacific. These upwelling locations are positioned above two compositionally- and seismologically-distinct[10] regions of the lowermost mantle that may organize global mantle flow[11] as they remain stationary over geologic time[12].

Viscous convection of Earth's mantle dissipates our planet's internal heat, and, because it mobilizes Earth's surface, is ultimately responsible for the Earth's long history of intense geological activity. Indeed, supercontinent formation and destruction[13], epeirogeny[4,5], mountain-building[6], intraplate volcanism[12], and plate tectonic motions[1-3] have been linked directly to viscous flow in the mantle. Yet, despite these close links, the outlines of present-day global mantle flow have only recently become delineated using tomographic images of the mantle's heterogeneous density structure to inform viscous flow modeling of the mantle[6,14]. Even this exercise has been complicated by the uncertain interpretation of mantle tomography, especially concerning the role of two large low shear-wave velocity provinces (LLSVPs) observed in the lowermost mantle beneath Africa and the Pacific[15]. While active upwelling from these regions helps explain patterns of seismic anisotropy[14], plate motions[3], orogeny[5,6], and long-wavelength topography[4], seismological constraints suggest that these regions are compositionally dense[16-18].

Under these conditions, thermochemical convection can help explain the geometry of upwellings[19], but their stability depends on the interaction of the LLSVP regions with mantle flow[20]. Our knowledge of mantle flow patterns is even poorer for past times, because direct geologic constraints on flow are few and past mantle density heterogeneity can only be inferred from time-reversed flow models[21] or inverse methods[22] based on present-day mantle structure, or subduction models that do not treat mantle upwelling[1].

Because they are ultimately linked to mantle convection, plate motions should contain information about the underlying mantle flow patterns. Indeed, shear tractions exerted by mantle flow on the lithospheric base may be a primary driver of plate motions[1-3] and thus directly link surface tectonics to interior dynamics. We can exploit this link for past times by utilizing tectonic reconstructions of plate motions, which are becoming increasingly better constrained[8,9], to infer patterns of past mantle flow. We achieve this by examining the net properties of plate motions, which should reflect the "average" response of Earth's lithosphere to long-wavelength viscous mantle flow. Previously, net rotation of the lithosphere (Fig 1a) has been linked to present-day mantle flow[14], but its utility for past times[8] may be limited because observations of net rotation are highly dependent on the choice of mantle reference frame. By contrast, the relative motions between plates are less dependent on reference frame and are of larger amplitude than net rotation rates. To exploit these attributes, we define several new metrics of relative plate motions that are useful for constraining the interaction between plate tectonics and mantle flow, and apply them to published reconstructions of plate motions both for present and past times.

We defined three new "net characteristics" of plate motions by performing different integrations of the tectonic plate motion vector field over the surface of the earth (see methods). The plate tectonic dipole vector **D** defines a "net convergence pole" toward which plates are moving in an average sense away from an antipodal "net divergence pole" (Fig. 1b). The plate tectonic quadrupole, defined by the quadrupole deformation matrix **Q** (see methods), describes a 2^{nd} order pattern of net plate motions associated with net hemispheric convergence toward two antipodal "positive" poles and divergence away from two antipodal "negative" poles located 90° away from the positive quadrupoles (Fig. 1c). This quadrupole motion occurs as revolution about two intermediate null poles (Fig. 1c). Plate tectonic net stretching, defined by deformation matrix **S** (see methods), describes convergence toward the two null poles of the quadrupole and divergence away from an equator midway between them (Fig. 1d). These net characteristics describe plate motions at the largest scales; they are influenced by both rapid regional-scale (e.g., northwestern North American convergence) and gradual global-scale deformations (e.g., the circum-Africa ridge system), but are dominated by the longest-wavelength large amplitude deformations.

We computed these net characteristics for present-day plate motions (Fig. 2a) and for vector fields associated with two major plate-driving forces: slab pull and basal shear tractions (Fig. 2b). The relevant pole locations for all three net characteristics (**D**, **Q**, and **S**) are approximately co-located for both plate motions and plate-driving forces. For example, dipole convergence of plate tectonics occurs in eastern Asia, dominated by convergent motion of the Pacific, Australian, Indian, African, and Eurasian plates toward this location (Fig. 2a). The fact that slab pull also converges on average toward this location (Fig. 2b) is perhaps not surprising because subduction results from plate convergence. The convergence of basal tractions toward eastern

Asia (Fig. 2b), however, reflects net motion of sub-lithospheric mantle flow toward this region. Within the mantle, downwelling occurs in this location (Fig. 2c), facilitated by a long history of subduction in the western Pacific that is observed tomographically[23]. The co-location of these dipoles thus not only indicates the importance of basal tractions for driving plate motions[1,3], but also illustrates a direct link between plate motions and global-scale patterns of mantle flow.

The quadrupole moments for plate motions, slab pull, and basal tractions are also aligned together (Fig. 2). In particular, quadrupole convergence for all three vector fields is centered in the western Pacific and South America (Fig. 2a), near regions of subduction and above major mantle downwellings (Fig. 2c). Similarly, quadrupole divergence is found in the central Pacific and eastern Africa (Fig. 2a,b), above major upwelling regions of the mantle (Fig. 2c) and just east of the location of the LLSVPs in the lowermost mantle (Fig. 2a). Poles orienting (negative) net stretching are also co-located near the geographic poles (Figs. 2a,b), which reflects the equatorial locations of the quadrupoles. As for the dipole, this co-location of quadrupoles reveals the direct link between surface plate motions and mantle flow patterns at depth. If we assume that this link also persisted for alternative plate configurations that existed in the past, then we can use dipole and quadrupole orientations computed for reconstructed past plate motions to infer the large-scale geometry of ancient mantle flow patterns.

To determine how dipole and quadrupole orientations have changed during Earth's recent history, we computed **D** and **Q** from a tectonic reconstruction of global plate motions for the past 150 Ma[8] that we have extended back to 250 Ma by combining paleomagnetic constraints on absolute and relative plate motions in the African hemisphere [24,25] with a reconstruction of the

Pacific basin[9]. The latter is largely synthetic (and thus uncertain) because all Triassic seafloor and any Jurassic hotspot tracks for the Pacific have been lost to subduction. Nevertheless, since 250 Ma dipole convergence has generally remained near eastern Asia (Fig. 3a), reflecting long-term stability of major downwelling beneath this area. Indeed, the stationary position of the Eurasian continent has been noted[26], and is consistent with persistent downwelling of slabs from the adjacent Panthalassa ocean. The central Pacific and eastern Africa positions of quadrupole divergence have also remained stable above the eastern edges of the LLSVPs (Fig. 3b), which is consistent with the long-term stability of upwelling in these areas. By contrast, the locations of quadrupole convergence have circumscribed Panthalassa, finally resting along its northwestern (and southeastern) edges during the late Cretaceous (Fig. 3b), about the time that subduction of increasingly younger lithosphere in the northern Pacific[9] may have diminished downwelling flow beneath this region. While migration of the convergent quadrupoles reflects changes in the dominant location of subduction-induced downwelling flow, the stationary nature of the divergent quadrupoles reflects stability of the two major mantle upwellings.

The positioning of mantle upwelling above the African and Pacific LLSVP regions of the lowermost mantle is consistent with flow patterns observed in thermochemical convection models[19]. Our observation that these upwellings have remained stably positioned above the current LLSVP regions may indicate that these LLSVPs form stable "anchors" that organize mantle flow and surface tectonics[11]. Indeed, plume ascent from the edges of the LLSVPs[12,20] has been used to define an absolute reference frame for plate motions[8] that allows paleogeography to be reconstructed into the deep past[24]. Our observation of quadrupole stability indicates that the two LLSVP regions have remained separate and in their current locations since at least the beginning of the Mesozoic, and were not forced into these locations by flow patterns governed by supercontinental surface tectonics since then[27]. Thus, if a transition from degree-1 to degree-2 convection occurred after the formation of Pangea[7] (i.e. after ~320 Ma), it probably occurred before ~250 Ma. The dipole and quadrupole amplitudes (Fig. S3) have been decreasing slowly and in concert since the mid-Mesozoic and do not exhibit evidence of a transition between dominant modes (Fig. S3). Dipole and quadrupole locations are also rarely co-located (Figs. 3, S6), which implies that the two systems are coupled to avoid degree-1 upwelling in the vicinity of degree-2 downwelling. Instead, persistent degree-2 upwelling arising from the two LLSVP structures may induce convergent flow in the lowermost mantle that consolidates these structures into their current geometries[20], thus protecting and isolating them over geological timescales[19]. The surface expression of this flow pattern is recorded in the geologic record of plate tectonics.

Methods Summary

Dipole. We define the "plate tectonic dipole" **D** as the direct integration of the plate motion velocity field **v** over the Earth's surface A_0 (Fig. S1):

$$\mathbf{D} = \frac{3}{2A_0}\int_{A_0} \mathbf{v}\, dA \qquad (1)$$

Here the normalization is chosen (see supplemental materials) so that the amplitude of **D** represents the magnitude of net motion on the equator midway between these poles (Fig. S2b).

Quadrupole and Net Stretching. Higher order net characteristics can be computed by integrating the outer product of the unit normal vector $\hat{\mathbf{r}}$ and **v** (Fig. S1), and separating the resulting tensor **L** into symmetric (**M**) and antisymmetric (**N**) components:

$$\mathbf{M}+\mathbf{N}=\mathbf{L}=\frac{1}{A_0}\int_{A_0}\hat{\mathbf{r}}\otimes\mathbf{v}\,dA \qquad (2)$$

Note that the diagonal components of **L** always sum to zero because $\mathrm{tr}(\mathbf{L})=\frac{1}{A_0}\int_{A_0}\hat{\mathbf{r}}\bullet\mathbf{v}\,dA$ and $\hat{\mathbf{r}}\perp\mathbf{v}$ everywhere (Fig. S1). The three independent components of **N** form the net rotation vector according to $R_k=3N_{ij}\varepsilon_{ijk}/2$ (see supplemental materials). The three eigenvalues of the symmetric **M** matrix ($\mu_1>\mu_2>\mu_3$) form the diagonalized matrix $\mathbf{M}_D$, which is simply **M** expressed in a coordinate system defined by the corresponding eigenvectors $\mathbf{m}_1$, $\mathbf{m}_2$, and $\mathbf{m}_3$. We can decompose $\mathbf{M}_D$ into "quadrupole" (**Q**) and "net stretching" (**S**) matrices as:

$$\mathbf{M}_D=\begin{bmatrix}\mu_1&0&0\\0&\mu_2&0\\0&0&\mu_3\end{bmatrix}=\frac{\mathbf{Q}}{6}+\frac{4\mathbf{S}}{15}=\frac{1}{6}\begin{bmatrix}Q&0&0\\0&0&0\\0&0&-Q\end{bmatrix}+\frac{4}{15}\begin{bmatrix}-S/2&0&0\\0&S&0\\0&0&-S/2\end{bmatrix} \qquad (3)$$

where the positive and negative elements of **Q** correspond to eigenvectors $\mathbf{m}_1$ and $\mathbf{m}_3$ respectively (Fig. 1c), and the unique (middle) element of **S** corresponds to eigenvector $\mathbf{m}_2$ (Fig. 1d). The piercing points of the eigenvectors $\pm\mathbf{m}_1$, $\pm\mathbf{m}_2$, and $\pm\mathbf{m}_3$ thus define the positive (convergent) quadrupoles, the net stretching poles (also null quadrupoles), and the negative (divergent) quadrupoles, respectively (Fig. 1c and 1d). We have defined $Q=6\mu_1+3\mu_2$ and $S=15\mu_2/4$ so that these values correspond to the maximum velocity magnitudes within the "pure" quadrupole and net stretching velocity fields (see supplemental material). Note that the net stretching deformation (Fig. 1d) reverses to become "net flattening" (polar extension and equatorial compression) if S<0 ($\mu_2<0$).

References

1 Lithgow-Bertelloni, C. & Richards, M. A. The dynamics of Cenozoic and Mesozoic plate motions. *Rev. Geophys.* 36, 27-78, doi:10.1029/97RG02282 (1998).

2 Stadler, G. *et al.* The dynamics of plate tectonics and mantle flow: From local to global scales. *Science* 329, 1033-1038, doi:10.1126/science.1191223 (2010).

3 van Summeren, J., Conrad, C. P. & Lithgow-Bertelloni, C. The importance of slab pull and a global asthenosphere to plate motions. *Geochemistry Geophysics Geosystems* 13, Q0AK03, doi:10.1029/2011gc003873 (2012).

4 Lithgow-Bertelloni, C. & Silver, P. G. Dynamic topography, plate driving forces and the African superswell. *Nature* 395, 269-272, doi:10.1038/26212 (1998).

5 Flowers, R. M., Ault, A. K., Kelley, S. A., Zhang, N. & Zhong, S. J. Epeirogeny or eustasy? Paleozoic-Mesozoic vertical motion of the North American continental interior from thermochronometry and implications for mantle dynamics. *Earth and Planetary Science Letters* 317, 436-445, doi:10.1016/j.epsl.2011.11.015 (2012).

6 Becker, T. W. & Faccenna, C. Mantle conveyor beneath the Tethyan collisional belt. *Earth and Planetary Science Letters* 310, 453-461, doi:10.1016/j.epsl.2011.08.021 (2011).

7 Zhang, N., Zhong, S. J., Leng, W. & Li, Z. X. A model for the evolution of the Earth's mantle structure since the Early Paleozoic. *Journal of Geophysical Research-Solid Earth* 115, B06401, doi:10.1029/2009JB006896 (2010).

8 Torsvik, T. H., Steinberger, B., Gurnis, M. & Gaina, C. Plate tectonics and net lithosphere rotation over the past 150 My. *Earth and Planetary Science Letters* 291, 106-112, doi:10.1016/j.epsl.2009.12.055 (2010).

9 Seton, M. *et al.* Global continental and ocean basin reconstructions since 200 Ma. *Earth-*

Science Reviews 113, 212-270, doi:10.1016/j.earscirev.2012.03.002 (2012).

10 Garnero, E. J. & McNamara, A. K. Structure and dynamics of Earth's lower mantle. *Science* 320, 626-628, doi:10.1126/science.1148028 (2008).

11 Dziewonski, A. M., Lekic, V. & Romanowicz, B. A. Mantle anchor structure: An argument for bottom up tectonics. *Earth and Planetary Science Letters* 299, 69-79, doi:10.1016/j.epsl.2010.08.013 (2010).

12 Torsvik, T. H., Smethurst, M. A., Burke, K. & Steinberger, B. Large igneous provinces generated from the margins of the large low-velocity provinces in the deep mantle. *Geophysical Journal International* 167, 1447-1460, doi:10.1111/j.1365-246X.2006.03158.x (2006).

13 Li, Z.-X. & Zhong, S. Supercontinent–superplume coupling, true polar wander and plume mobility: Plate dominance in whole-mantle tectonics. *Physics of the Earth and Planetary Interiors* 176, 143-156, doi:10.1016/j.pepi.2009.05.004 (2009).

14 Conrad, C. P. & Behn, M. D. Constraints on lithosphere net rotation and asthenospheric viscosity from global mantle flow models and seismic anisotropy. *Geochemistry Geophysics Geosystems* 11, Q05W05, doi:10.1029/2009GC002970 (2010).

15 Lassak, T. M., McNamara, A. K., Garnero, E. J. & Zhong, S. J. Core-mantle boundary topography as a possible constraint on lower mantle chemistry and dynamics. *Earth and Planetary Science Letters* 289, 232-241, doi:10.1016/j.epsl.2009.11.012 (2010).

16 Kennett, B. L. N., Widiyantoro, S. & van der Hilst, R. D. Joint seismic tomography for bulk sound and shear wave speed in the Earth's mantle. *J. Geophys. Res.* 103, 12469-12493, doi:10.1029/98jb00150 (1998).

17 Ishii, M. & Tromp, J. Normal-mode and free-air gravity constraints on lateral variations in

velocity and density of Earth's mantle. *Science* 285, 1231-1236, doi:10.1126/science.285.5431.1231 (1999).

18 Deschamps, F. & Trampert, J. Mantle tomography and its relation to temperature and composition. *Physics of the Earth and Planetary Interiors* 140, 277-291, doi:10.1016/j.pepi.2003.09.004 (2003).

19 McNamara, A. K., Garnero, E. J. & Rost, S. Tracking deep mantle reservoirs with ultra-low velocity zones. *Earth and Planetary Science Letters* 299, 1-9, doi:10.1016/j.epsl.2010.07.042 (2010).

20 Bower, D. J., Gurnis, M. & Seton, M. Lower mantle structure from paleogeographically constrained dynamic Earth models. *Geochemistry, Geophysics, Geosystems* 14, 44-63, doi:10.1029/2012GC004267 (2013).

21 Steinberger, B. & O'Connell, R. J. Changes of the Earth's rotation axis owing to advection of mantle density heterogeneities. *Nature* 387, 169-173, doi:10.1038/387169a0 (1997).

22 Liu, L. J., Spasojevic, S. & Gurnis, M. Reconstructing Farallon Plate subduction beneath North America back to the Late Cretaceous. *Science* 322, 934-938, doi:10.1126/science.1162921 (2008).

23 Ritsema, J., van Heijst, H. J. & Woodhouse, J. H. Global transition zone tomography. *J. Geophys. Res.* 109, B02302, doi:10.1029/2003jb002610 (2004).

24 Torsvik, T. H., Müller, R. D., Van der Voo, R., Steinberger, B. & Gaina, C. Global plate motion frames: Toward a unified model. *Reviews of Geophysics* 46, RG3004, doi:10.1029/2007rg000227 (2008).

25 Steinberger, B. & Torsvik, T. H. Absolute plate motions and true polar wander in the absence of hotspot tracks. *Nature* 452, 620-623, doi:10.1038/nature06824 (2008).

26 Collins, W. J. Slab pull, mantle convection, and Pangaean assembly and dispersal. *Earth and Planetary Science Letters* 205, 225-237, doi:10.1016/s0012-821x(02)01043-9 (2003).

27 Zhong, S. J., Zhang, N., Li, Z. X. & Roberts, J. H. Supercontinent cycles, true polar wander, and very long-wavelength mantle convection. *Earth and Planetary Science Letters* 261, 551-564, doi:10.1016/j.epsl.2007.07.049 (2007).

28 DeMets, C., Gordon, R. G., Argus, D. F. & Stein, S. Effect of recent revisions to the geomagnetic reversal time scale on estimates of current plate motions. *Geophys. Res. Lett.* 21, 2191-2194, doi:10.1029/94GL02118 (1994).

29 Wu, B. J., Conrad, C. P., Heuret, A., Lithgow-Bertelloni, C. & Lallemand, S. Reconciling strong slab pull and weak plate bending: The plate motion constraint on the strength of mantle slabs. *Earth and Planetary Science Letters* 272, 412-421, doi:10.1016/j.epsl.2008.05.009 (2008).

30 Naliboff, J. B., Conrad, C. P. & Lithgow-Bertelloni, C. Modification of the lithospheric stress field by lateral variations in plate-mantle coupling. *Geophysical Research Letters* 36, L22307, doi:10.1029/2009GL040484 (2009).

Supplementary Information accompanies the paper and consists of an 11-page document that details the net characteristic normalizations and the extension of the tectonic model back to 250 Ma, includes supplementary figures S1-S6, and describes two separate supplemental files that contain the stage poles and plate boundaries of the 150-250 Ma plate motion reconstruction.

Acknowledgments. We thank two anonymous reviewers for helpful comments, NSF CAREER grant EAR-1151241 (C.P.C.) and ERC grant 267631 (T.H.T.) for support, and the Norwegian Centre for Advanced Study in Oslo for making this collaboration possible.

Author Contributions. C.P.C. defined the method to compute net characteristics, B.S. and T.H.T. extended the plate reconstruction through the Mesozoic, all authors developed the geologic application and interpretation, C.P.C. prepared the manuscript with input, comments and review from all authors.

Additional Information. The authors declare no competing financial interests. Correspondence and requests for materials should be addressed to C.P. Conrad (Dept. Geology & Geophysics, SOEST, University of Hawaii, 1680 East-West Road, Honolulu, HI 96822, USA; clintc@hawaii.edu).

FIGURE LEGENDS

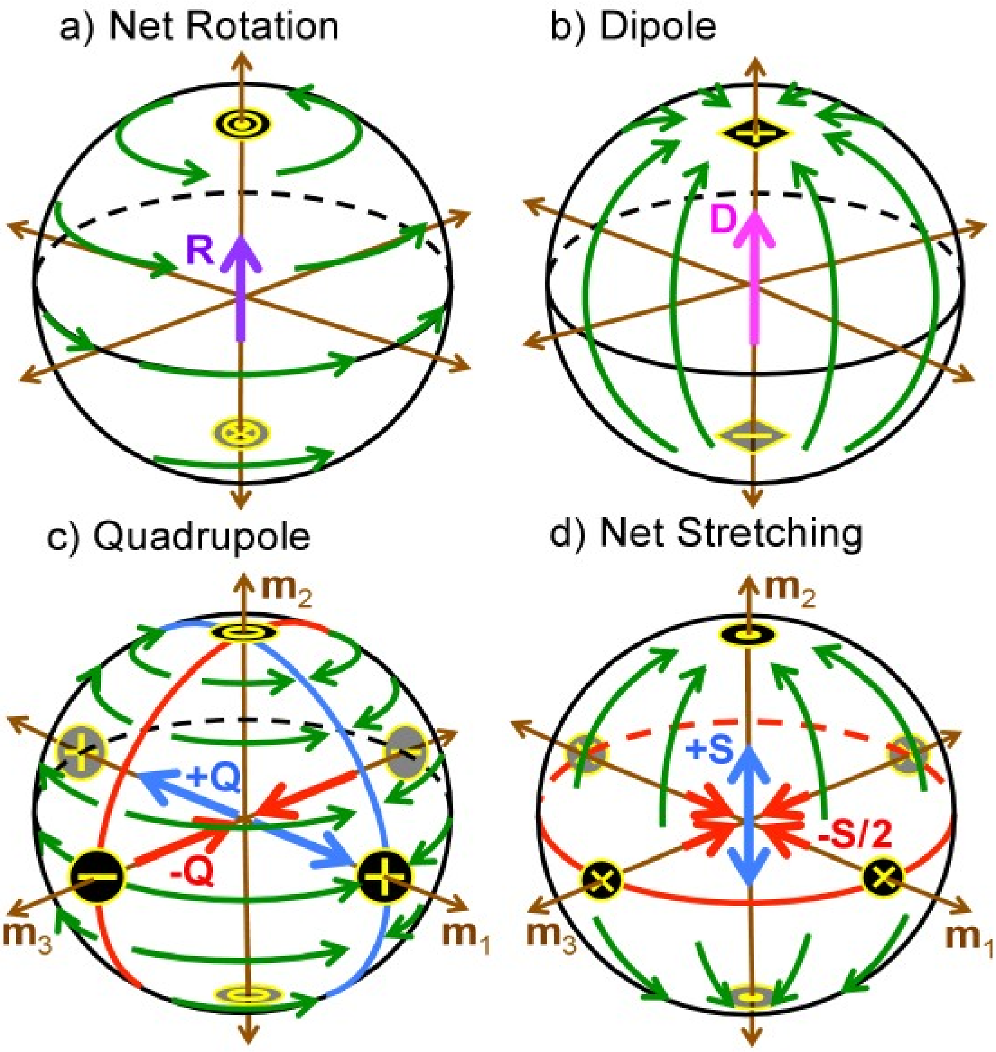

Figure 1. Definitions of net characteristics. Plate motions for (a) net rotation, (b) net dipole, (c) net quadrupole, and (d) net stretching (green arrows, see Fig. S2), their net characteristic vector definitions (**R**, **D**, **±Q**, and **+S**, respectively, and the $\mathbf{m}_1$, $\mathbf{m}_2$, and $\mathbf{m}_3$ eigenvectors; see methods), and the symbols used to denote pole locations: encircled dot or cross for positive or negative net rotation poles (a), plus or minus within a diamond for positive or negative dipoles (b), plus, circle or minus signs within a circle for positive, null, or negative quadrupoles (c), and dots or crosses for compressive or extensional net stretching poles (d).

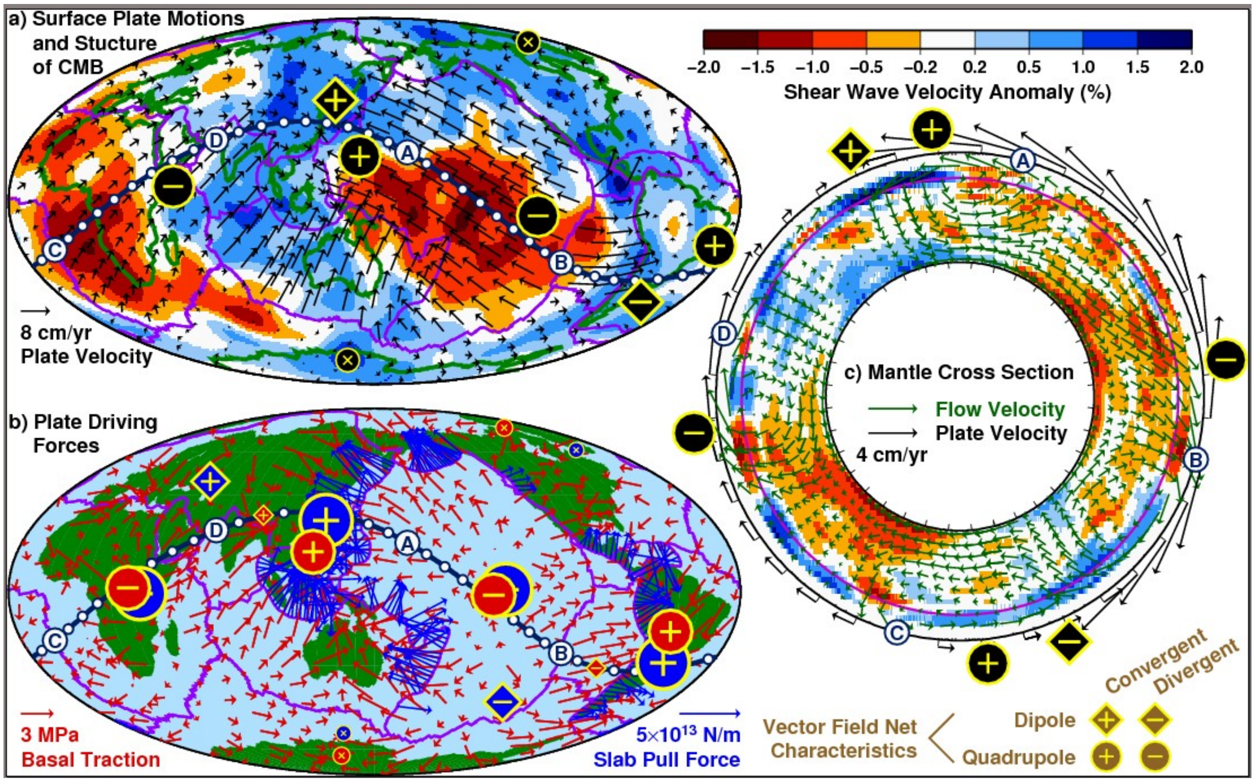

Figure 2. **Association of plate tectonic net characteristics with those of underlying mantle flow.** Net characteristic pole locations (symbols as in Fig. 1) for the dipole, quadrupole, and net stretching components of (a) present-day plate motions[28] (black symbols) and (b) estimates for plate tectonic driving forces associated with slab pull[29] (blue symbols) and basal tractions on plates[30] (red symbols). A mantle cross section (c) cutting through great circle ABCD (drawn on maps) shows tomographic shear velocity anomaly[23] (colors, also drawn in map view in (a) at 2800 km depth), the associated mantle flow field[14] (green arrows), surface plate motion (black arrows), and net characteristic dipole and quadrupole locations for plate motions (black symbols).

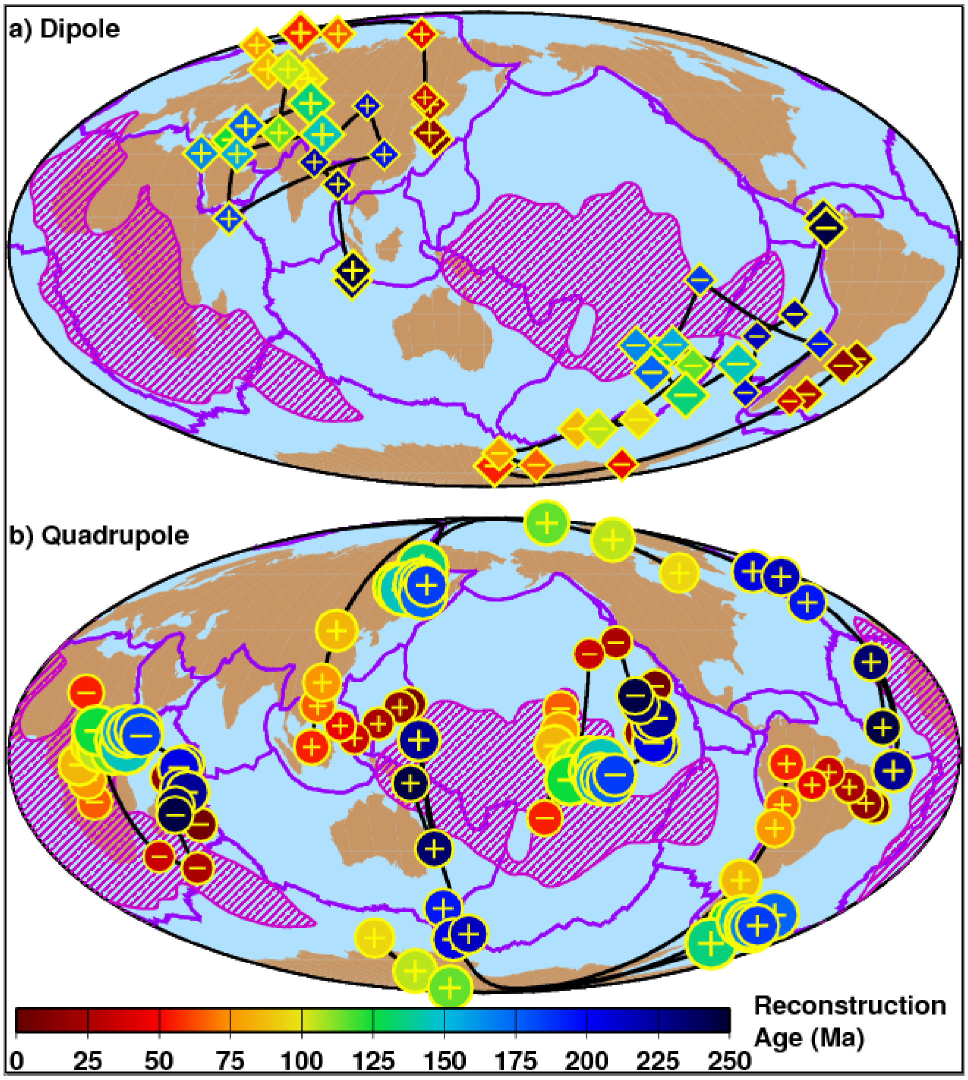

Figure 3. Temporal evolution of plate tectonic net characteristics. Plate tectonic (a) dipole and (b) quadrupole locations as a function of age for a reconstruction of plate motions since the Triassic (Fig. S6). Symbols as in Fig. 1, with colors indicating reconstruction age and sizes indicating dipole or quadrupole magnitude (Fig. S3). Note the stability of (a) the plate tectonic dipole near eastern Asia and (b) the divergent (negative) quadrupole above the western edges of the two LLSVPs (denoted here as pink hatches showing where shear waves at 2800 km are >1% slow[12]) beneath Africa and the Pacific. Alternative reconstructions[9] (Figs. S4, S5) show similar stability of these features.

Supplementary Materials:

Stability of Active Mantle Upwelling Revealed by Net Characteristics of Plate Tectonics

Clinton P. Conrad[1*], Bernhard Steinberger[2,3], Trond H. Torsvik[3,4,5]

[1] Dept. Geology & Geophysics, SOEST, University of Hawaii at Manoa, Honolulu, HI 96822, USA
[2] Helmholtz Centre Potsdam, GFZ German Research Centre for Geosciences, 14473 Potsdam, Germany
[3] Centre for Earth Evolution and Dynamics (CEED), University of Oslo, 0316 Oslo, Norway
[4] Geodynamics, Geological Survey of Norway, NO-7491, Trondheim, Norway
[5] School of Geosciences, University of Witwatersrand, WITS 2050, South Africa
* Corresponding Author (clintc@hawaii.edu)

1.0 Net Characteristic Normalizations

For any vector field on a sphere $\mathbf{v}(\theta,\varphi)$, where θ is colatitude and φ is longitude (Fig. S1), we can compute several net characteristics of that field by integrating $\mathbf{v}$ over the surface of the sphere. The vector and tensor definitions of four net characteristics (net rotation, net dipole, net quadrupole, and net stretching) are defined in the Methods Summary in the main text, but their magnitudes are determined by the normalization chosen for each net characteristic function. Here we define normalization factors that yield net characteristic amplitudes that correspond to the maximum velocity of a representative velocity field for each net characteristic (Fig. S2).

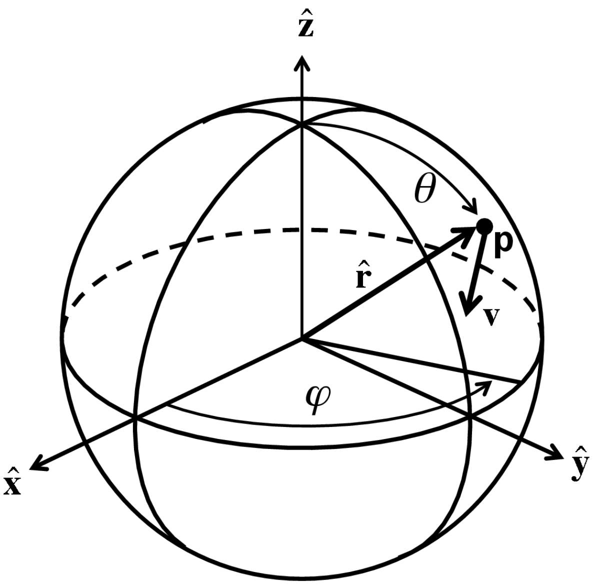

Figure S1. Spherical (θ, φ, r), and Cartesian (x, y, z) reference frames, and an arbitrary point **p** on the Earth's surface ($r = R_E$) moving with velocity $\mathbf{v}(\theta,\varphi)$.

1.1 Net Rotation

Solid body net rotation about the north pole (Fig. 1a) can be expressed as an eastward-oriented velocity field with amplitude that depends on θ as $v_\theta = 0$ and $v_\varphi = v_R \sin\theta$, where v_R is the maximum velocity amplitude occuring at $\theta = \pi/2$ (on the equator). This vector field is exemplified in Fig. S2a, where v_R=5 cm/yr. In Cartesian coordinates this velocity is expressed as $\mathbf{v} = \left(-v_R \sin\theta\sin\varphi, v_R \sin\theta\cos\varphi, 0\right)$. The net rotation vector $\mathbf{R}$ is calculated by crossing the local normal $\hat{\mathbf{r}} = \left(\sin\theta\cos\varphi, \sin\theta\sin\varphi, \cos\theta\right)$ with $\mathbf{v}$ and integrating, following the definition of $\mathbf{R}$ given by *Ricard et al.* [1991]:

$$\mathbf{R} = \frac{3}{2A_0}\int_{A_0} \hat{\mathbf{r}} \times \mathbf{v}\, dA = \frac{3v_R\hat{\mathbf{z}}}{2(4\pi)}\int_0^{2\pi}\int_0^{\pi} \sin^3\theta\, d\theta\, d\phi = v_R\hat{\mathbf{z}} \qquad \text{(S1)}$$

Thus, the magnitude of the net rotation vector, $\mathbf{R}$, is equal to v_R, which is the net rotation velocity occurring along the net rotation equator (Fig. S2a).

Note that the net rotation vector **R** can also be obtained from the antisymmetric matrix **N** (defined in eq. 2). We can show this by writing (2) as:

$$\mathbf{L}=\frac{1}{A_0}\int_{A_0}\hat{\mathbf{r}}\otimes\mathbf{v}dA=\frac{1}{A_0}\int_{A_0}\begin{bmatrix} r_x v_x & r_x v_y & r_x v_z \\ r_y v_x & r_y v_y & r_y v_z \\ r_z v_x & r_z v_y & r_z v_z \end{bmatrix}dA \tag{S2}$$

Then the symmetric (**M**) and antisymmetric (**N**) components of **L**=**M**+**N** are:

$$\mathbf{M}=\frac{1}{2A_0}\int_{A_0}\begin{bmatrix} 2r_x v_x & r_x v_y+r_y v_x & r_x v_z+r_z v_x \\ r_y v_x+r_x v_y & 2r_y v_y & r_y v_z+r_z v_y \\ r_z v_x+r_x v_z & r_z v_y+r_y v_z & 2r_z v_z \end{bmatrix}dA \quad \mathbf{N}=\frac{1}{2A_0}\int_{A_0}\begin{bmatrix} 0 & r_x v_y-r_y v_x & r_x v_z-r_z v_x \\ r_y v_x-r_x v_y & 0 & r_y v_z-r_z v_y \\ r_z v_x-r_x v_z & r_z v_y-r_y v_z & 0 \end{bmatrix}dA \tag{S3}$$

Note that the cross product components of the net rotation vector **R** from (S1) can be re-expressed in terms of the components of the anti-symmetric matrix **N**:

$$R_k=3N_{ij}\varepsilon_{ijk}/2 \tag{S4}$$

where ε_{ijk} is the Levi-Civita permutation symbol. Thus, the components of the antisymmetric matrix **N** define the net rotation vector **R**.

1.2 Net Dipole

A pure dipole vector field with a (positive) convergence pole at the north pole (Fig. 1b) has the form $v_\theta=-(v_D\sin\theta)$ and $v_\varphi=0$ (Fig. S2b), or $\mathbf{v}=-v_D\sin\theta(\cos\theta\cos\varphi,\cos\theta\sin\varphi,-\sin\theta)$ in Cartesian coordinates (Fig. S2b). Applying **v** to the definition of the net dipole in (1) gives:

$$\mathbf{D}=\frac{3}{2A_0}\int_{A_0}\mathbf{v}\,dA=\frac{3v_D\hat{\mathbf{z}}}{2(4\pi)}\int_0^{2\pi}\int_0^{\pi}\sin^3\theta\,d\theta\,d\phi=v_D\hat{\mathbf{z}} \tag{S5}$$

Thus, the magnitude of the dipole vector **D** is equal to v_D, which is the maximum poleward velocity, occurring along the dipole equator (Fig. S2b).

1.3 Net Quadrupole

We define the quadrupole velocity field, with positive (convergent), intermediate (null), and negative (divergent) poles (defined by the $\mathbf{m}_1$, $\mathbf{m}_2$, and $\mathbf{m}_3$ eigenvectors, respectively) coincident with **y**-, **z**-, and **x**-axes, respectively (Fig. 1c). In this case $v_\theta=0$ and $v_\varphi=v_Q\sin\theta\sin2\varphi$, or $\mathbf{v}=v_Q(-\sin\theta\sin2\varphi\sin\varphi,\sin\theta\sin2\varphi\cos\varphi,0)$ in a Cartesian system (Fig. S2c). Integration of the outer product (S2) yields:

$$\mathbf{L}=\frac{v_Q}{A_0}\int_0^{2\pi}\int_0^{\pi}\begin{bmatrix}\sin\theta\cos\varphi\\ \sin\theta\sin\varphi\\ \cos\theta\end{bmatrix}\begin{bmatrix}-\sin\theta\sin\varphi\sin2\varphi & \sin\theta\cos\varphi\sin2\varphi & 0\end{bmatrix}\sin\theta\,d\theta\,d\varphi=\frac{v_Q}{6}\begin{bmatrix}-1&0&0\\0&1&0\\0&0&0\end{bmatrix} \tag{S6}$$

Solving for **Q** by diagonalizing **M** and applying (3) as described in the main text, we find:

$$\mathbf{Q}=\begin{bmatrix}v_Q&0&0\\0&0&0\\0&0&-v_Q\end{bmatrix} \tag{S7}$$

where the corresponding eigenvectors $\mathbf{m}_1$, $\mathbf{m}_2$, and $\mathbf{m}_3$ are parallel to the **y**, **z**, and **x** axes, respectively (Fig. 1c, S2c), producing divergence poles at ($\theta = \pi/2$, $\varphi = 0$) and ($\pi/2$, π), convergent poles at ($\pi/2$, $\pm\pi/2$) and intermediate poles at $\theta = 0$ and $\theta = \pi$. The quadrupole amplitude in (S7) is $Q=v_Q$, and thus is equal to that field's largest vector magnitude, which occurs midway between the convergent and divergent poles (Fig. S2c).

1.4 Net Stretching

We define the positive net stretching velocity field as convergent toward both the north and south poles, and divergent away from the equator (Fig. 1d). In this case $v_\theta = -v_S \sin 2\theta$ and $v_\varphi = 0$, which is $\mathbf{v} = -v_S \sin 2\theta \left(\cos\theta\cos\varphi, \cos\theta\sin\varphi, -\sin\theta\right)$ in a Cartesian system (Fig. S2d). Again rewriting the outer product using (S2) and integrating, we find:

$$\mathbf{L} = \frac{v_S}{A}\int_0^{2\pi}\int_0^{\pi} \sin 2\theta \begin{bmatrix} \sin\theta\cos\varphi \\ \sin\theta\sin\varphi \\ \cos\theta \end{bmatrix} \begin{bmatrix} -\cos\theta\cos\varphi & -\cos\theta\sin\varphi & \sin\theta \end{bmatrix} \sin\theta \, d\theta \, d\varphi = \frac{4v_S}{15}\begin{bmatrix} -1/2 & 0 & 0 \\ 0 & -1/2 & 0 \\ 0 & 0 & 1 \end{bmatrix} \quad \text{(S8)}$$

Solving for **S** by diagonalizing **M** and applying (3) as described in the main text (assuming that net stretching occurs in the presence of a larger quadrupole field to associate net stretching with the intermediate $\mathbf{m}_2$ eigenvector, as discussed below), we find:

$$\mathbf{S} = \begin{bmatrix} -v_S/2 & 0 & 0 \\ 0 & v_S & 0 \\ 0 & 0 & -v_S/2 \end{bmatrix} \quad \text{(S9)}$$

where the associated eigenvectors $\mathbf{m}_1$, $\mathbf{m}_2$, and $\mathbf{m}_3$ are parallel to the **y**, **z**, and **x** axes, respectively (Figs. 1d, S2d). The resulting net stretching expressed by (S9) yields convergence poles at the piercing points of $\pm\mathbf{m}_2$ ($\theta = 0$ and $\theta = \pi$), and divergence away from the equator ($\theta = \pi/2$). The net stretching magnitude is thus $S=v_S$, which is again the maximum velocity within the pure net stretching field (Fig. S2d), occurring at $\theta = \pi/4$ and $\theta = 3\pi/4$. If $S=v_S$ is negative, then the sense of motion is reversed to produce "net flattening" with diverging intermediate poles (at $\theta = 0$ and $\theta = \pi$) and convergence toward the equator.

2.0 Separating the Quadrupole and Net Stretching Components

Note that our method for separating $\mathbf{M}_D$ into quadrupole and net stretching components is not unique. We have chosen to align the positive and negative quadrupole vectors (+**Q** and –**Q**) with $\mathbf{m}_1$ and $\mathbf{m}_3$ (Fig. 1c), which correspond to the most positive and most negative eigenvalues of **M** (μ_1 and μ_3, respectively), and the net stretching vector (+**S**) with $\mathbf{m}_2$ (Fig. 1d), which is associated with the intermediate eigenvalue (μ_2). However, we could have alternatively associated net stretching with the largest (μ_1) or smallest (μ_3) eigenvalues, which would distribute the deformation between the quadrupole and net stretching differently. For example, associating net stretching (+**S**) with $\mathbf{m}_3$ and the quadrupole vectors (+**Q** and –**Q**) with $\mathbf{m}_1$ and $\mathbf{m}_2$ changes (3) to:

$$\mathbf{M}_D = \begin{bmatrix} \mu_1 & 0 & 0 \\ 0 & \mu_2 & 0 \\ 0 & 0 & \mu_3 \end{bmatrix} = \frac{\mathbf{Q}}{6} + \frac{4\mathbf{S}}{15} = \frac{1}{6}\begin{bmatrix} Q & 0 & 0 \\ 0 & -Q & 0 \\ 0 & 0 & 0 \end{bmatrix} + \frac{4}{15}\begin{bmatrix} -S/2 & 0 & 0 \\ 0 & -S/2 & 0 \\ 0 & 0 & S \end{bmatrix} \quad \text{(S10)}$$

where $Q = 6\mu_1 + 3\mu_3$ and $S = 15\mu_3/4$. Applying this alternative method for separation to a pure quadrupole field for which $\mu_1 = v_Q/6$, $\mu_2 = 0$, and $\mu_3 = -v_Q/6$ (see above), we find new amplitudes for the quadrupole and net stretching components (specifically, we find $Q = v_Q/2$ and $S = -5v_Q/8$), and different orientations of the net quadrupole and net stretching vectors compared to our original method. Both methods accurately express the deformation described by $\mathbf{M}_D$ and associated eigenvectors, but do so in different ways. Our method of aligning the intermediate eigenvector ($\mathbf{m}_2$) with net stretching associates the largest amplitude eigenvalues (and the associated $\mathbf{m}_1$ and $\mathbf{m}_3$ eigenvectors) with quadrupole motion. For global plate motions, quadrupole motion tends to dominate (Fig. S3), which makes our choice of separation method convenient. Regardless of the method, however, the second order net characteristics computed using (2) are uniquely described by the eigenvectors $\mathbf{m}_1$, $\mathbf{m}_2$, and $\mathbf{m}_3$, and their associated eigenvalues. Our method consistently aligns these eigenvectors with the positive quadrupole (**+Q**), net stretching (**+S**), and negative quadrupole (**-Q**) poles, respectively, and thus fully and uniquely describes the second order net characteristics of plate tectonic motions.

3.0 Extension of the *Torsvik et al.* [2010] Reconstruction back to 250 Ma, and Comparison with other Reconstructions

Torsvik et al. [2010] reconstructed plate motions globally back to 150 Ma (Fig. S6a-o), but reconstructed continental areas (i.e. all plates except for those in the Pacific basin) back to 250 Ma. To extend *Torsvik et al.'s* [2010] model back to 250 Ma for all areas, we used the global reconstruction of *Seton et al.* [2012] to reconstruct the motion of plates in the Pacific basin for the 150-200 Ma time period (Fig. S6p-t) and extended these Pacific plate motions for the 200-250 Ma time period (Fig. S6u-y) using the data archive supplementing *Seton et al.* [2012]. Poles of rotation and plate boundaries for the 150-250 Myr time period are included here as supplemental files and can be added to those published by *Torsvik et al.* [2010] to produce a global reconstruction back to 250 Ma.

Due to the lack of hotspot tracks, absolute plate motions in the Pacific basin, and hence the contribution of this basin to the plate tectonic dipole, are rather unconstrained for the entire 150-250 Ma period. *Seton et al.* [2010] assume that the Pacific plate - then a small plate at a triple junction - was fixed. Before ~180 Ma, relative plate motions for the Pacific, and therefore their contribution to the plate tectonic quadrupole, are also rather unconstrained, as no ocean floor is preserved before this time. *Seton et al.* [2010] assume that spreading away from the Pacific basin triple junction had been ongoing before 180 Ma. Before 230 Ma, their model assumes that the Farallon plate was fixed to North America.

The main differences between the models of *Torsvik et al.* [2010] and *Seton et al.* [2012] are that (1) the former use independent Pacific and African hotspot reference frames, whereas the latter use a plate circuit linking both hemispheres after 83 Ma, and that (2) *Torsvik et al.* [2010] use a simplified model of Pacific plate motions prior to 83 Ma. Different from *Seton et al.* [2012], *Doubrovine et al.* [2012] determine an absolute reference frame that fits hotspot tracks globally after 83 Ma. However, because *Seton et al.* [2012] and *Doubrovine et al.* [2012] were otherwise constructed similarly, their dipole and quadrupole results also look similar (compare Figs. S4 and

S5), apart from a small shift due to their slightly differing absolute reference frames. *van der Meer et al.* [2010] suggest a westward shift of the reference frame peaking at 18° at 150 Ma. Applying a corresponding shift to the dipole and quadrupole locations would move divergent quadrupoles closer to the LLSVP centers.

Similarities and differences between these models help to characterize model uncertainties and to assess which model features are robust. The main uncertainty of our analysis comes from the fact that an increasingly smaller fraction of the ocean floor is preserved for older time periods, which means that the plate configuration for an increasingly larger fraction of the Earth's surface must be "best guessed". This missing fraction is referred to as "world uncertainty" by *Torsvik et al.* [2010], and reaches 60 % at 150 Ma. Given this, it would be difficult, and probably also misleading, to state formal uncertainties of our dipole and quadrupole locations. However, comparison between results for the different models presented here (Figs. 3, S4, S5) indicates that the location and stability of both the dipole axis and the quadrupole divergence are robust. The models also agree that quadrupole convergence poles moved from more polar locations earlier towards more equatorial locations since the late Cretaceous, but differ somewhat in the rate and path of motion prior to the mid-Cretaceous.

4.0 Additional Supplemental Files: Digital Plate Boundaries & Rotation Poles (150-250 Ma)

Two additional files provide the lat-long locations of (1) digitized plate boundaries and (2) plate rotation stage poles for each plate for each 10 Myr interval between 150 and 250 Ma. The format of these files is that same as that of similar files provided for 0-150 Ma by *Torsvik et al.* [2010]. Indeed these files extend *Torsvik et al.'s* [2010] model back to 250 Ma (Fig. S6).

5.0 References Cited in Supplementary Materials

Doubrovine, P. V., Steinberger, B., and Torsvik, T. H. Absolute plate motions in a reference frame defined by moving hot spots in the Pacific, Atlantic, and Indian oceans, *Journal of Geophysical Research* 117*,* B09101, doi:10.1029/2011jb009072 (2012).

Duncan, R. A., & Clague, D. A. Pacific plate motion recorded by linear volcanic chains, in *The Ocean Basins and Margins*, *vol. 7A*, *The Pacific Ocean*, ed. by A. E. A. Nairn et al., pp. 89–121, Plenum, New York, doi:10.1007/978-1-4613-2351-8_3, (1985).

Koppers, A. A. P., Morgan, J. P., Morgan, J. W., & Staudigel, H. Testing the fixed hot spot hypothesis using ^{40}Ar/^{39}Ar age progressions along seamount trails, *Earth and Planetary Science Letters* 185, 237–252, doi:10.1016/S0012-821X(00)00387-3 (2001).

Ricard, Y., Doglioni, C., & Sabadini, R. Differential rotation between lithosphere and mantle: A consequence of lateral mantle viscosity variations, *Journal of Geophysical Research* 96, 8407-8415, doi:10.1029/91jb00204 (1991).

Seton, M., Müller, R. D., Zahirovic, S., Gaina, C., Torsvik, T., Shephard, G., Talsma, A., Gurnis, M., Turner, M., Maus, S., & Chandler, M. Global continental and ocean basin reconstructions since 200 Ma, *Earth-Science Reviews* 113, 212-270, doi:10.1016/j.earscirev.2012.03.002 (2012).

Torsvik, T. H., Steinberger, B., Gurnis, M., & Gaina, C. Plate tectonics and net lithosphere rotation over the past 150 My, *Earth & Planetary Sci. Lett.* 291, 106-112, doi:10.1016/j.epsl.2009.12.055 (2010).

van der Meer, D. G., Spakman, W., van Hinsbergen, D. J. J., Amaru, M. L., & Torsvik, T. H., Towards absolute plate motions constrained by lower-mantle slab remnants, *Nature Geoscience* 3, 36-40, doi:10.1038/ngeo708 (2010).

Wessel, P., & Kroenke, L. Pacific absolute plate motion since 145 Ma: An assessment of the fixed hot spot hypothesis, *Journal of Geophysical Research* 113, B06101, doi:10.1029/2007JB005499 (2008).

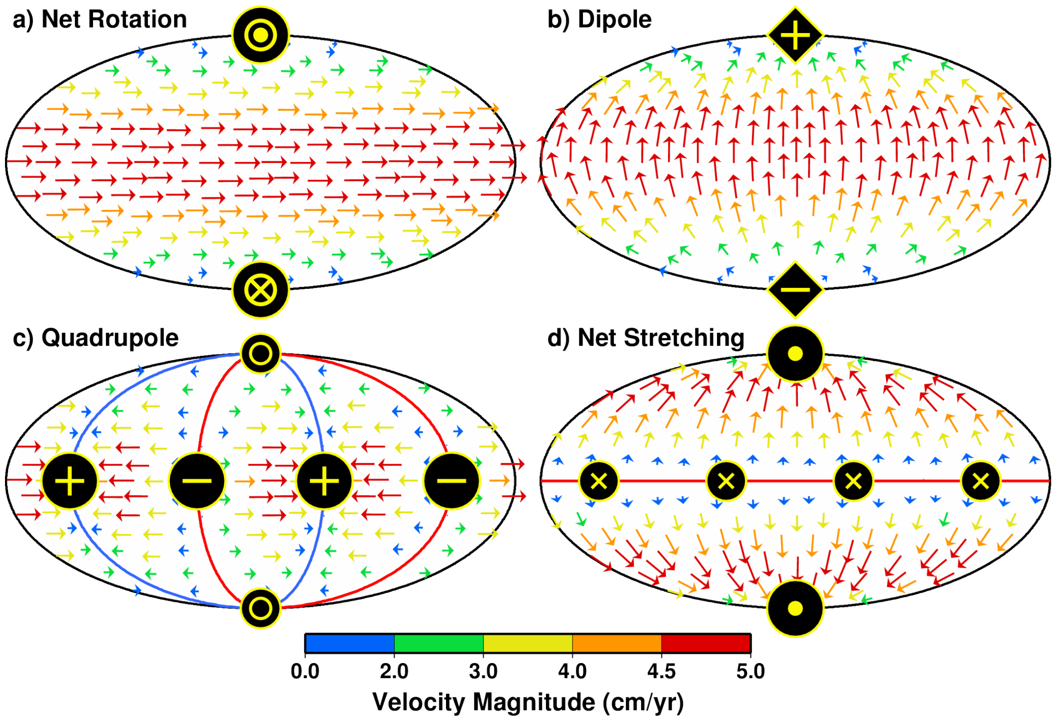

Figure S2. Representative velocity fields for (a) net rotation, (b) net dipole, (c) net quadrupole, and (d) net stretching, with functional forms as described in the text. Velocity direction is shown by arrows, and their length and color correspond to velocity magnitude. The maximum velocity magnitude in each case is 5 cm/yr, which also corresponds to the net characteristic magnitude for each case. The locations of net characteristic poles are denoted by symbols consistent with those defined in Fig. 1.

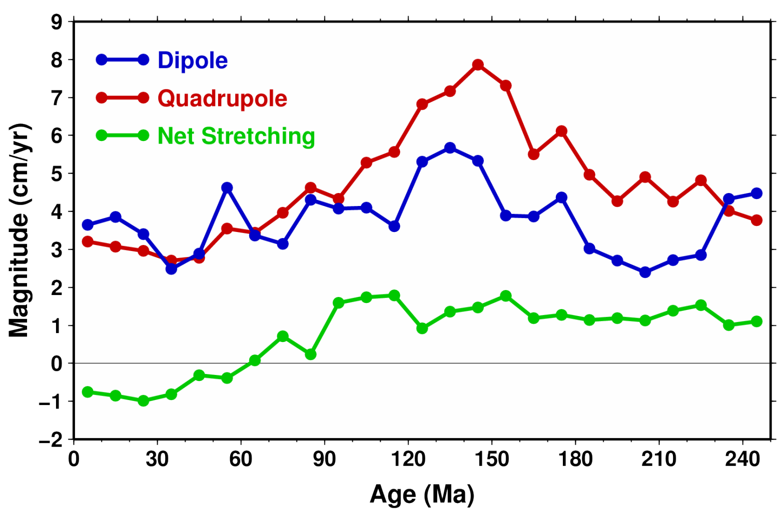

Figure S3. Magnitude of three net characteristic components (net dipole, net quadrupole, and net stretching as blue, red, and green lines) as a function of tectonic reconstruction age (Figs. 3, S6).

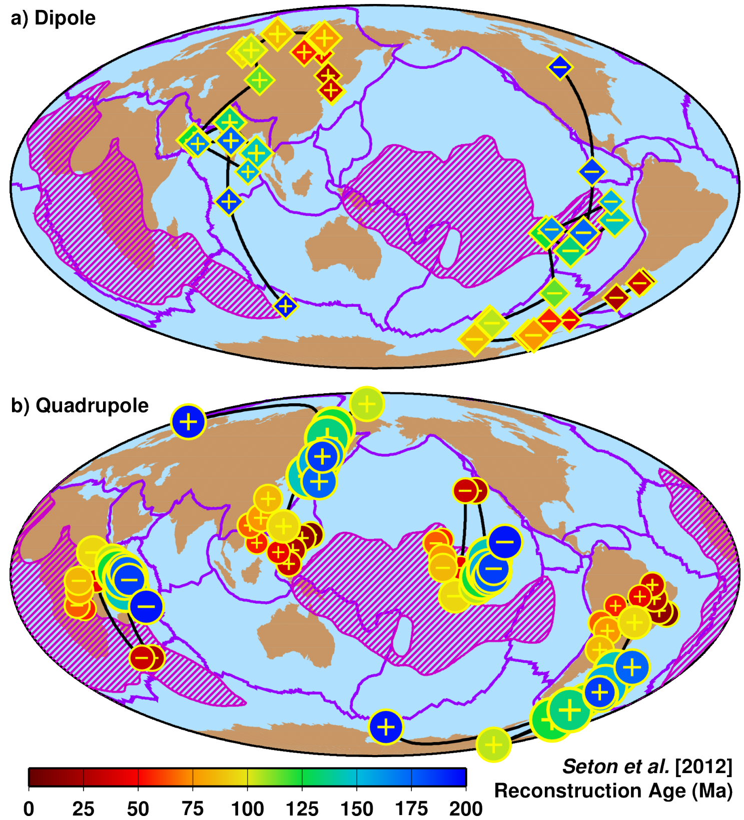

Figure S4. Motion of (a) dipole and (b) quadrupole net characteristic poles as a function of reconstruction age (similar to Fig. 3), but computed for the reconstruction of *Seton et al.* [2012], which extends back to 200 Myr.

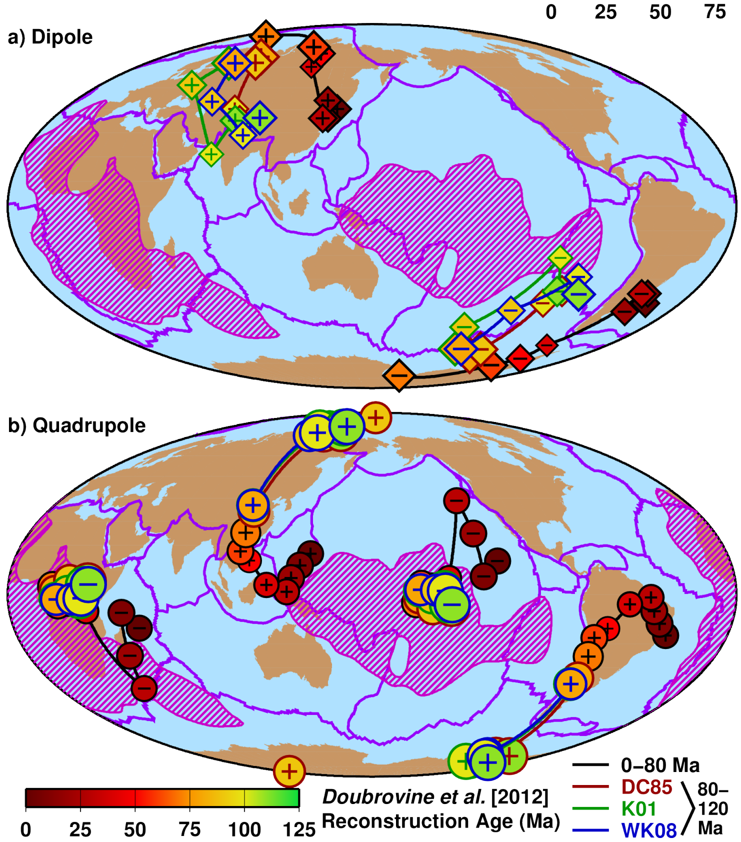

Figure S5. Motion of (a) dipole and (b) quadrupole net characteristic poles as a function of reconstruction age (similar to Fig. S4), but computed for the reconstruction of *Doubrovine et al.* [2012], which extends to 120 Ma. *Doubrovine et al.* [2012] presents three models for the 80-120 Ma timeframe, based on *Duncan & Clague* [1985], *Koppers et al.* [2001], and *Wessel & Kroenke* [2008] (which we denote as DC85, K01, and WK08, respectively). Here these three models can be distinguished by the color of the symbol boundary (red, green, and blue for DC85, K01, and WK08, respectively) for symbols in the 80-120 Ma timeframe. Black symbol outlines are used for the 0-80 Ma timeframe, for which *Doubrovine et al.* [2012] presents only one model.

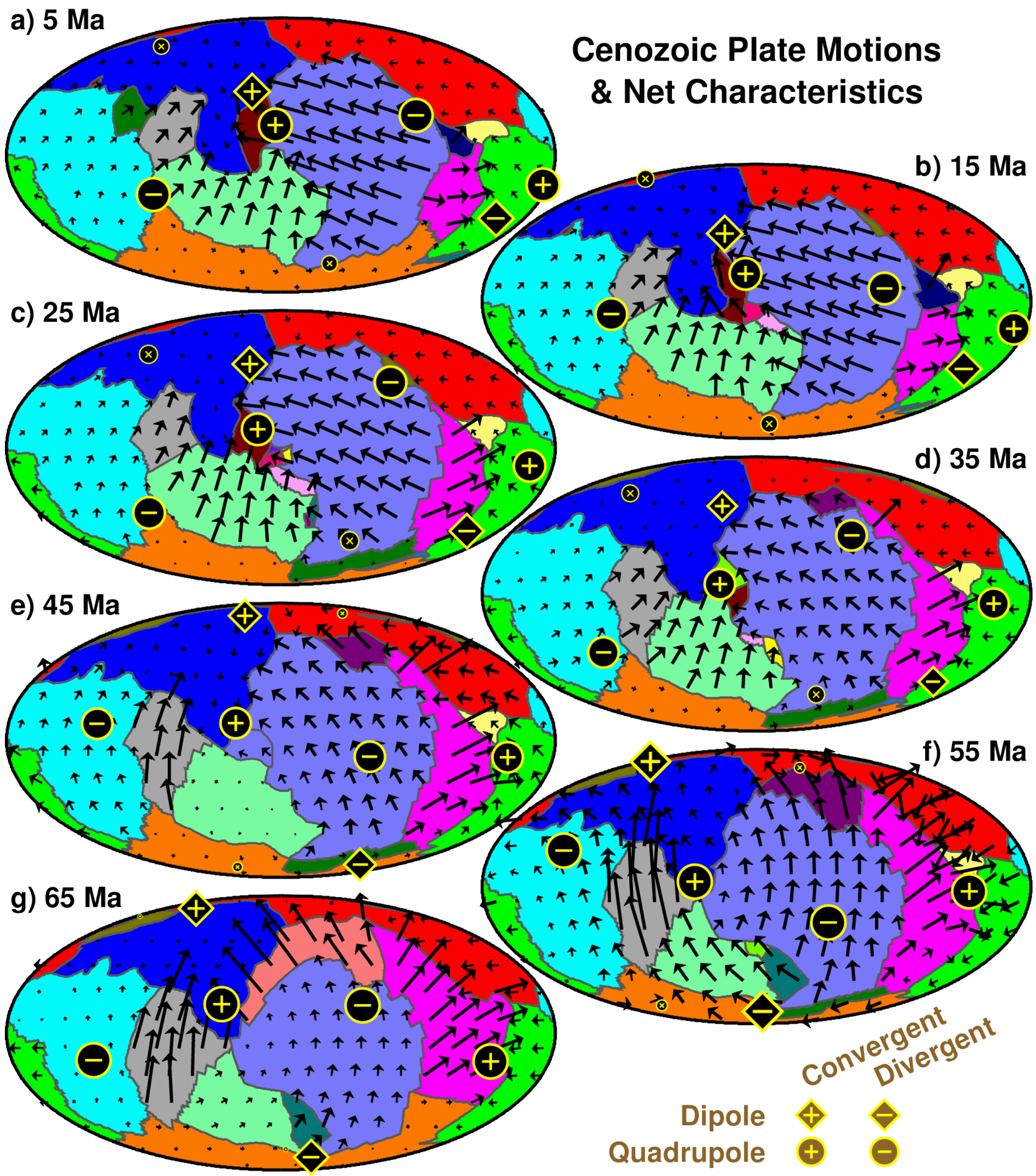

Figure S6. Plate motions (arrows) and computed net characteristic poles (symbols) for the Cenozoic (a-g), Cretaceous (h-o), Jurassic (p-t), and Triassic (u-y) time periods, based on the tectonic reconstruction of *Torsvik et al.* [2010] for the past 150 Ma, and extended back to 250 Ma by reconstructing the Pacific basin following *Seton et al.* [2012]. Reconstructions are in 10 Myr intervals (labeled age denotes middle of interval) over which plate motions are averaged.

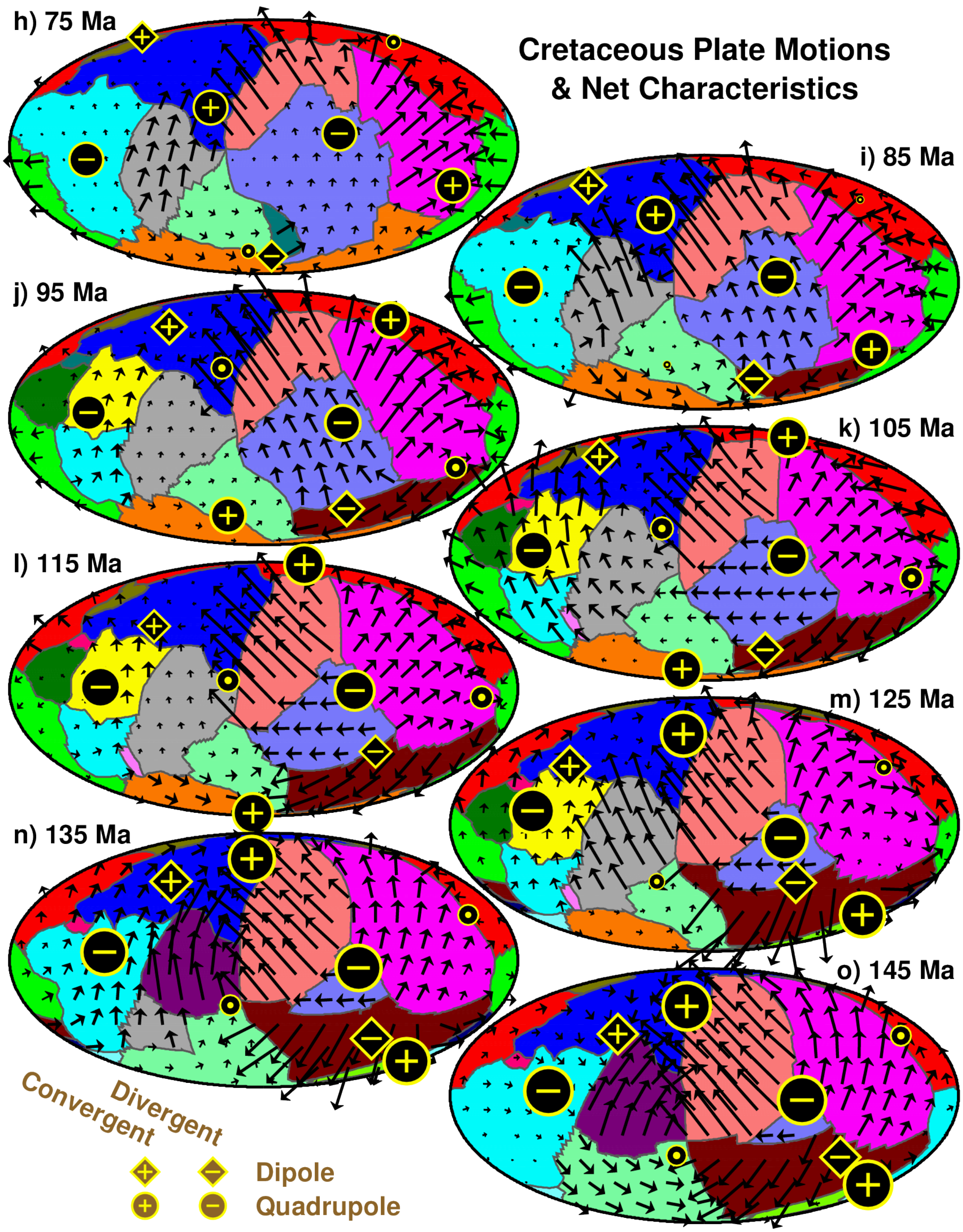

Figure S6. (continued, shown here for the Cretaceous)

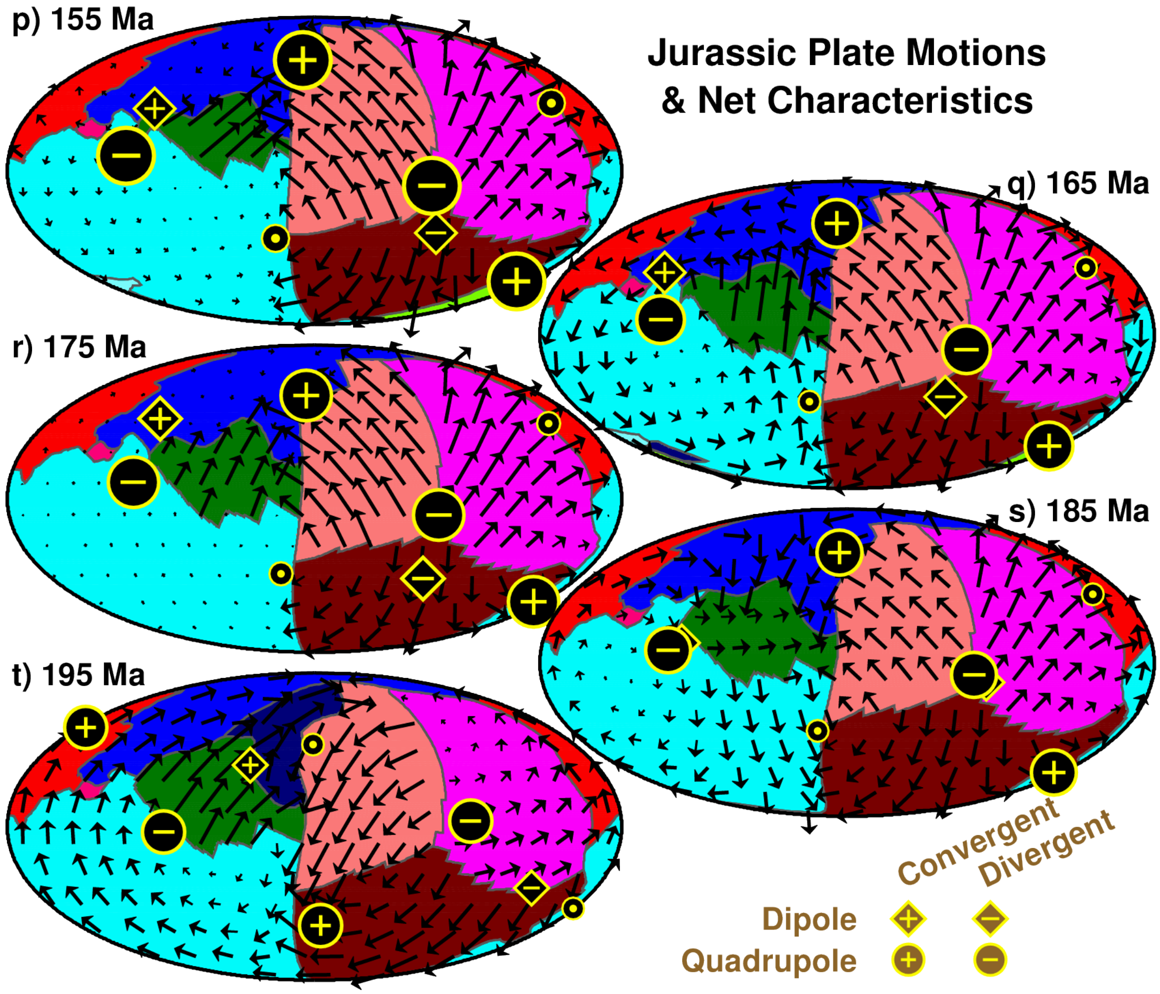

Figure S6. (continued, shown here for the Jurassic)

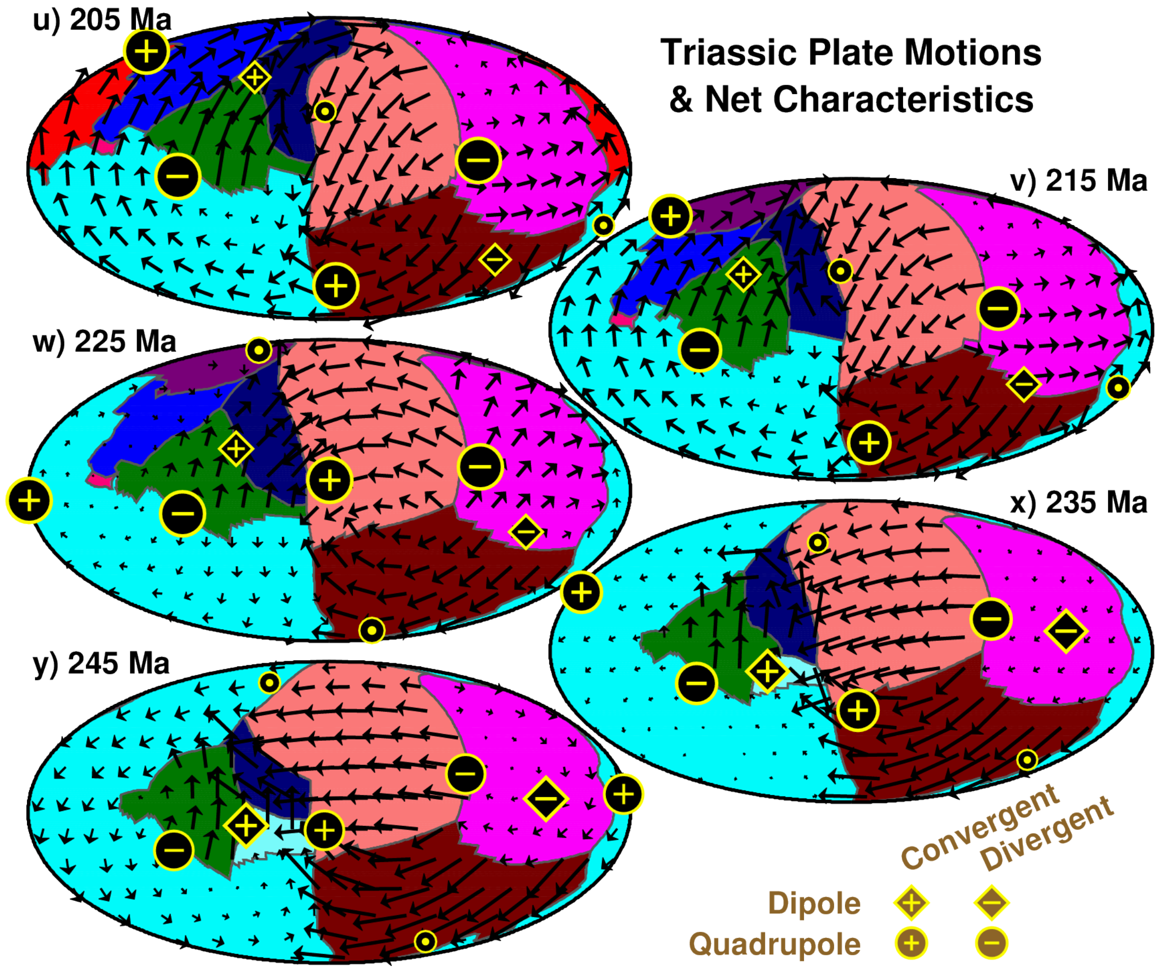

Figure S6. (continued, shown here for the Triassic)